Characteristics and mechanisms of near-surface atmospheric electric field negative anomalies preceding the 5 September, 2022, Ms6.8 Luding earthquake, China

Lixin Wu[1, 2], Xiao Wang[1, 2], Yuan Qi[1, 2], Jingchen Lu[1, 2], Wenfei Mao[1, 2]

[1] School of Geosciences and Info-Physics, Central South University, Changsha, 410083, China

5 [2] Laboratory of Geo-Hazards Perception, Cognition and Predication, Central South University, Changsha, 410083, China

Correspondence to: Yuan Qi (weloveqy@163.com)

Abstract. A Ms6.8 strike-slip earthquake (EQ) occurred in Luding, Sichuan province, China, on 5 September, 2022, causing great losses to the surrounding Ganzi Prefecture and Ya'an City. In this research, the near-surface atmospheric electric field (AEF), recorded at four discretely distributed sites 15d before the Luding EQ, were analyzed and

10 discriminated by using multi-source auxiliary data including precipitation, cloud base height and low cloud cover, and nine possible seismic AEF anomalies at four sites were obtained preliminarily. Accordingly, surface microwave brightness temperature (MBT), which is very sensitive to the surface dielectrics and closely related to the air ionization, together with surface soil moisture, lithology, and 3D-simulated crustal stress field, was jointly analyzed for confirming the seismic relations of the obtained negative AEF anomalies. The geophysical environment for crustal

15 high-stress concentration, positive charge carriers transfer and surface accumulation was demonstrated to exist and satisfy the conditions of generating locally the negative AEF anomalies. Furthermore, to deal with the spatial disparities in sites and regions with potential atmospheric ionization, the data of near-surface wind field was employed to scrutinize the reliability of the AEF anomalies by comprehensively considering the spatial relationships among surface charges accumulation areas, wind direction and speed, as well as the AEF site. Finally, four negative

20 AEF anomalies were deemed to be closely related to the Luding EQ, and the remaining five anomalies were ruled out. The mechanism of negative AEF anomalies before the Luding EQ were believed to be: positive charge carriers were generated from the underground high stress concentration areas, and then transferred to and accumulated on the ground surface and to ionize the surface air, thus disturbing the aground AEF. This study offers an approach to identify and analyze the seismic AEF anomalies, and is also helpful to study the pre-shocking coupling process between

25 coversphere and atmosphere.

Keywords: atmospheric electric field, seismic anomaly, P-holes, microwave brightness temperature, crustal stress field alteration

1 Introduction

30 In the state of nature, the operation of Global Electric Circuit (GEC) is driven by global thunderstorm activity and large-scale ion separation in charged cloud (Rycroft et al., 2000). In the background of GEC, a direct current (DC) atmospheric field with an amplitude of around 130 V/m is always present in global non-thunderstorm or sunny areas (Sun,1987). This electric field, also known as the fair-weather atmospheric electric field (FW-AEF), is oriented vertically downwards, which means that the atmosphere is positively charged while the ground is negatively charged.

35 In recent decades, some scientists have discovered that seismic activity can cause AEF anomalies with its direction opposite to FW-AEF in the seismogenic region. In 1966, Kondon (1966) detected pre-earthquake (EQ) abnormal electric field signal by using the field mill electric field instrument for the first time at the Matsushiro Observatory in Japan. Based on the electric field data recorded by Pixian site and Wenjiang site (in Chengdu, China), significant abnormal phenomena of AEF before the 2008 Ms8.0 Wenchuan EQ were found when the interference of lightning

40 activities were excluded (Li et al.,2017). Chen et al. (2022) also observed the AEF anomalies before the 2021 Ms4.3 Luanzhou EQ at two sites in Baodi and Yongqing, China. By analyzing the meteorological data, the anomalous signal

monitored at Baodi station was found to be influenced by a combination of transit clouds and geological activity, while the bay-type persistent electric field anomaly monitored at Yongqing station was considered as a typical AEF precursor of the EQ.

45   At present, there are three acceptable mechanisms for AEF anomalies before EQs. It is considered that seismic-related anomaly in radon emanation can be linked to preseismic electromagnetic phenomena such as the great changes of small ion concentration and AEF (Omori et al., 2007). In recent study (Jin et al., 2020), the AEF reduction before the Wenchuan EQ was interpreted from the perspective of the rapid changing of radon concentration as the mainshock approaching. Besides, by combining the time series and dynamic periodogram of AEF anomalies from 6 hours before

50 to 6 hours after the EQ, Yasuhide et al. (2022) attributed the phenomenon to the internal gravity waves generated near the epicenter passing through the AEF site, which changed the space charge density in the surface layer of the atmosphere. In addition, during the experimental study, Freund (2000, 2010) found that stress-activated carriers, named as P-holes, activated in the igneous and metamorphic rocks, are able to transfer along stress gradient and accumulate on the rock surface in unstressed areas or even on the ground surface covered by sands. When the P-holes

55 arrive at the air-ground interface, a positive potential could be produced and air particles here are able to be ionized so as to change the near-surface AEF when it reached a high level (Freund, 2013). Besides, the accumulation of P-holes on ground surface was also believed to reduce the surface microwave dielectric constant and enhance the regional microwave radiation (Mao et al., 2020; Qi et al., 2021a, 2021b).

    Meanwhile, some other researchers have also proposed different opinions on the pre-EQ AEF anomalies observed

60 at ground sites. Based on the statistical analysis of 103 pre-EQ bay-type AEF anomalies in the Kamchatka region, Smirnov et al. (2019) found that the duration and magnitude of AEF anomalies in hour-scale did not depend on either the magnitude of the EQ or the distance to the epicenter, while that in day-scale were related to the magnitude of the EQ. Hao et al., (1988) analyzed the AEF at the three stations in Baijiatong, Baodi and Beidaihe for several seismic events happened in and around Beijing from 1977 to 1986, and found that there were evident negative anomalies of

65 AEF variation before the EQs, decaying significantly with the distance to the epicenter and being associated only with nearby EQs but not far strong EQs. However, most of the researches were based on statistical judgements and have not yet integrated with the regional geological conditions of seismogenious zone as well as the local crustal stress field alteration (CSFA), which is crucial to whether charges from the stressed rock mass of Earth's crust can ionize the near-surface atmosphere.

70   It's well known that atmospheric vertical electric field is the bridge connecting the surface charges and atmospheric particle concentration, and the current consensus is that the increased concentration of atmospheric ions at the ground-air interface leads to the formation of additional vertical electric fields, which further transport ions from the lower atmosphere to the upper atmosphere, ultimately causing atmospheric anomalies. In our recent research, the multi-parameter seismic anomalies before the 2015 Nepal EQ sequence were analyzed systematically (Wu et al., 2023) by

75 referring to the lithosphere–coversphere–atmosphere (LCA) coupling paradigm (Wu et al., 2009, 2012) and lithosphere–coversphere–atmosphere-ionosphere (LCAI) coupling paradigm (Qin et al., 2013). However, due to lack of AEF observations before and during the two major EQs, the abnormal changes in atmospheric particles, such as aerosols and humidity, cannot be well linked to the changes in parameters of ground surface, such as microwave brightness temperature (MBT), thus the coupling process between the coversphere and atmosphere was not presented

80 perfectly. Fortunately, in the seismogenic zone of the Luding EQ in 2022, the potential AEF disturbances before the EQ were recorded at four stations, which provided an excellent chance to study the abnormal features of AEF aroused by EQ. In this study, the characteristics of the pre-seismic AEF vibration were analyzed, and the relations between the AEF anomalies and the Luding EQ were identified carefully by using multi-source auxiliary data. Finally, the mechanism of the seismic AEF anomalies was discussed by analyzing surface MBT anomaly and three-dimensional

85 crustal stress distribution, and four of the nine potential AEF anomalies were ultimately determined to be EQ related.

2 Study area and data sources

2.1 Study area

The Ms6.8 Luding EQ, happened in Luding County, Sichuan Province, China, at 12:52 on 5 September 2022 (Beijing Time), with its epicenter located at 29.59°N, 102.09°E and a hypocenter depth of 14.5 km (Yang et al., 2022).

90 The EQ occurred near the southeast Moxi section of the Xianshuihe fault (XSHF), which is a left-slip fault between the Bayan Har Block and the Sichuan-Yunnan Block (Ji et al., 2020). The study area was selected as [99°~106° E, 28°~32° N] in consideration of the epicenter and the geographical locations of the AEF instrument, in which there are Longmenshan faults (LMSF), the Anninghe fault (ANHF), the Longquanshan fault (LQSF) and the XSHF developed. The GAR, GUZ and SWG for AEF observations locate nearby the XSHF while LES locates east to the

95 southwest section of the LQSF. Figure 1 shows a complete overview of the study area.
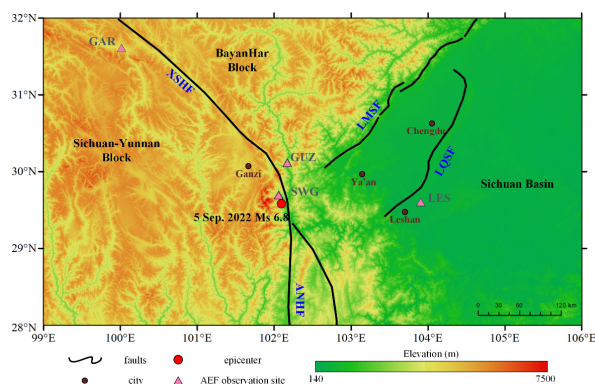
Figure 1. Distribution of the AEF observation sites and topography in the study area. Background image is the digital elevation derived from Shuttle Radar Topography Mission (SRTM) datasets

2.2 Data sources

100 #### 2.2.1 Atmospheric electric field observations

The GAR, GUZ and SWG were deployed by National Space Science Centre of Chinese Academy of Sciences with instrument EMF-100 (Li, 2022), and the LES was deployed by China University of Geosciences (Wuhan) with instrument CS110 (Chen et al.,2021). The specific information of AEF sites is shown in Table 1. The GAR is located in a highland area in the southeast of Ganzi County, at an altitude of 3356 m above sea level (masl). The GUZ is

105 located in Guzan Township, Kangding City, at an altitude of 1421 masl in the saddle, with the Dadu River flowing through it on the east side. The SWG is located in a valley in Yanzigou Town, Luding County, at an altitude of 2125 masl. The LES is located in Leshan City, with an altitude of 401 masl in the plain area, with flat terrain around it.

Table 1. Key information about the AEF observation sites

Site name	Longitude	Latitude	Distance from the epicenter	Sampling frequency	Unit
GAR	100.02° E	31.61° N	298.97 km		
GUZ	102.17° E	30.12° N	59.29 km	1 s	kV m⁻¹
SWG	102.07° E	29.69° N	11.20 km		
LES	103.91° E	29.60° N	175.67 km		

The intensity of AEF is measured according to the principle that a conductor can generate an induced-charge in an electric field. If a metallic conductor with surface area S_c is exposed to an electrostatic field of electric field strength E, the charge density ϕ of the induced-charge generated on its surface can be expressed as:

$$\phi = \varepsilon_0 KE \tag{1}$$

where ε_0 represents the air dielectric constant and K is the electric field distortion coefficient. The induced-charge Q can be expressed as:

$$Q = \phi S_C = \varepsilon_0 KES_C \tag{2}$$

$$E = \frac{Q}{\varepsilon_0 KS_C} \tag{3}$$

Therefore, if the amount of induced-charge is measured, the strength of the AEF can be obtained. When a metallic conductor is connected to the earth, an electric current will be generated. It is known from electrical knowledge that if the conductor generates a continuously varying induced-charge, the measured intensity of the induced-current can be expressed as:

$$I = \frac{dQ}{dt} \tag{4}$$

The AEF meter sensor uses a moving piece and a stator to produce a continuously changing induced-charge. As the moving piece begins to rotate, the stator is periodically exposed to the electric field or shielded under the moving piece and the two-stage circuit will receive a current signal of equal magnitude and opposite direction (Ji, 2022). Therefore, E can be deduced by measuring the intensity of the induced-current:

$$E = \frac{Q}{\varepsilon_0 KS_C} = \frac{\int Idt}{\varepsilon_0 KS_C} \tag{5}$$

2.2.2 Meteorological data and MBT

The AEF is to be influenced by a variety of factors, including not only meteorological factors such as clouds, rain, snow and lightning, but also the factors of global space weather activity such as geomagnetic disturbances, solar activity (Sun,1987). In order to accurately identify whether the anomalous signals are caused by an EQ, it is necessary to eliminate each of the potential influencing factors. In this research, the meteorological data used is from the ERA5 reanalysis provided by the European Centre for Medium-Range Weather Forecasts, including low cloud cover (LCC), cloud base height (CBH), total precipitation (TP), and wind field. The LCC refers to the proportion of clouds in the grid that are 2 km about below, CBH refers to the height of the lowest cloud base above the Earth's surface, TP is the cumulative value of liquid and frozen water falling on the Earth's surface over a period of time, and wind field includes the wind speed (WS) and direction at a height of 10m aground (Hersbach et al., 2023). The space weather data used includes the geomagnetic index Dst from the World Geomagnetic Centre (WGC) and the sunspot numbers (SSN) from ESA.

The MBT data and surface soil moisture (SSM) data were also used to exclude local drought factors, and to analyze the potential accumulation of positive charges for the generation of AEF anomalies. MBT data is obtained from the high-performance microwave radiometer AMSR-2 on board GCOM-W1, which is available at five microwave frequencies, 10.65, 18.7, 23.8, 36.5 and 89 GHz, in both horizontal and vertical polarization (Imaoka et al., 2012). SSM data is derived from the GLDAS data set, which represents a measure of moisture in the soil at a depth of 0~10 cm below the ground surface (Rodell et al., 2004). Details of all the data used are shown in Table 2.

Table 2. Multi-source data for AEF anomaly discrimination.

Dataset	Data source	Temporal resolution	Spatial resolution	Unit
Low cloud cover (LCC)	ERA5	1 h	0.25°×0.25°	/
Cloud base height (CBH)				km

Total precipitation (TP)				mm
Wind field				m s^{-1}
Dst	WGC	1 h	/	/
Sunspot number	ESA	1 d	/	/
Microwave brightness temperature (MBT)	AMSR-2	1 d	50 km×50 km	K
Surface soil moisture (SSM)	GLDA V.2.1	3 h	0.25°×0.25°	kg m^{-2}

3 Results and analysis

3.1 Characteristics of local fair-weather AEF

The FW-AEF is an important background characterizing the periodic variation of natural AEF in a particular region. It is necessary to study the characteristics of the FW-AEF to better identify seismic AEF anomalies. At present, the screening criteria for FW-AEF (Israelsson et al., 2001; Harrison et al., 2018) cannot be fully standardized and need to be modified in conjunction with the local topographical features, meteorological disturbances and geographical environment around the site. In this study, the following screening criteria were set for obtaining FW-AEF: 1) no daytime rainfall, 2) low cloud cover closing to zero, 3) no thunderstorms, 4) wind speed less than 8 m s^{-1} at 10 m aground, and 5) no long period of negative AEF anomalies (to exclude anthropogenic influence and other uncertain factors). The AEF data from 1 May, 2022 to 30 September, 2022 for GAR, GUZ, SWG and 1 August 2022 to 30 September 2022 for LES were analyzed based on the data availability. After filtering and processing the AEF data, the daily variation curves of FW-AEF for the four sites were then obtained as in Figure 2.
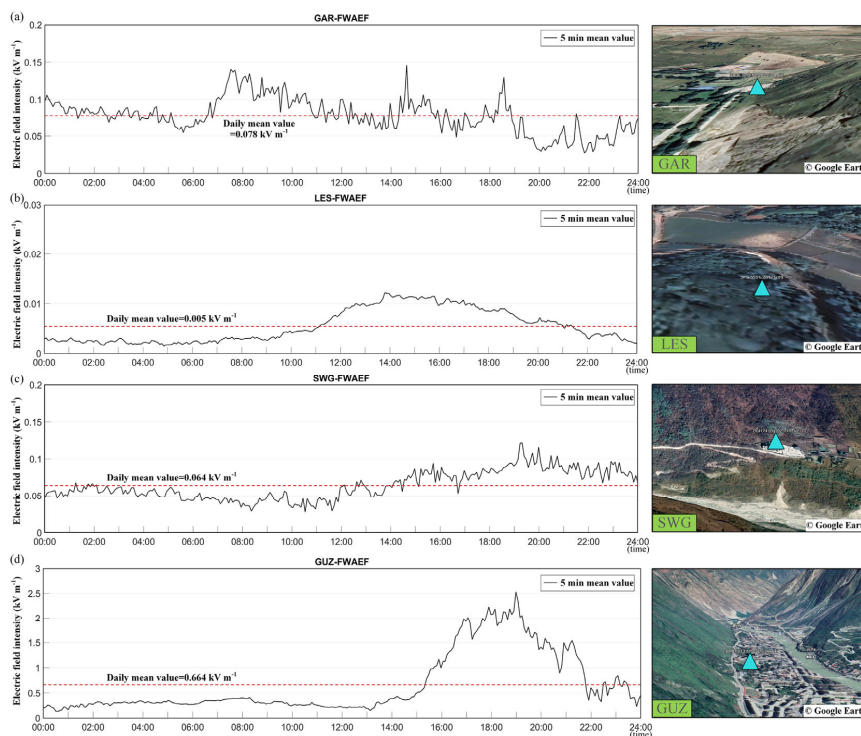
Figure 2. Daily variation of FW-AEF and Google Earth images at four different sites of GAR (a), LES (b), SWG (c), and GUZ (d).

160   Figure 2 shows the 5-minute mean curve (left) of FW-AEF and satellite image from Google Earth (right). Overall, the FW-AEF curve of GAR is characterized by a single peak and two valleys, which displayed a shallow valley of 0.023 kV m^{-1} around 06:30, and then showed a quick rise and reached the peak with 0.23 kV m^{-1} between 07:00 and 08:00, following by a gradual decline. The second valley appeared between 19:00 and 20:00 with a valley of 0.015 kV m^{-1} at GAR. The FW-AEF at LES varied more gently and behaved a single-peaked pattern, which showed a peak

165   of 0.012 kV m^{-1} at around 14:00. The AEF values of SWG and GUZ changed slightly before 12:00, but increased gradually to a peak about 0.14 kV m^{-1} for SWG and 2.7 kV m^{-1} for GUZ around 19:10. The FW-AEF of SWG and GUZ were both single-peaked. The peak of the FW-AEF curve of GUZ is much higher, which may be attributed to the particular topography of river valley and the greater impact of human activity in the town.

3.2 Identification of potential seismic AEF anomalies

170   Lightning, haze, meteorological events such as clouds and rain, and space weather events such as magnetic storms and solar activity are able to lead to changes in AEF. Global space weather events such as geomagnetic disturbances (Kleimenova et al., 2008) and solar activity (Tacza et al., 2018) can also affect the AEF. This research used the *Dst* and *SSN* to represent the intensity of geomagnetic activity and solar activity, respectively. Figure 3(a) shows the amount of daily change in the two indices. According to the international practice, *Dst* < -50 and > -30 represents

175   weak magnetic storm activity, while *SSN* > 40 and < 80 represents moderate solar activity. The magnetic storms and solar activity were not strong enough to cause a prolonged negative AEF anomalies from 22 August to 5 September, 2022, so the effect of such factors on the AEF can be ruled out in this study.

To exclude the influences of meteorology and space activities on the AEF, this research conducted a time-series analysis of multiple remote sensing data (CBH, LCC and TP) on an hourly or daily mean basis. For the time period

180   of negative AEF anomalies, remote sensing data was selected to judge whether the non-seismic factors (meteorological parameters) existed synchronously, as shown in Figure 3(b-j). The daily variation curves of AEF from 22 August to 5 September and the hourly graphs of CBH, LCC and TP for the corresponding periods were retrieved, and nine time periods of negative AEF anomalies with possible seismic activity factors were screened out from all the four sites, being 4 anomalies for GAR, 4 anomalies for LES and 1 anomaly for SWG.

185   For GAR, the AEF curve on 22 and 23 August were not so different, with both negative AEF anomalies occurring twice during daytime. The first AEF anomaly appeared before 9:00, without low cloud and precipitation, which indicates that it had been influenced by seismic activity. The second negative anomaly appeared between 12:00 and 18:00, with a small amount of precipitation at the beginning accompanied with a sudden drop in the height of cloud base and a rise in the amount of low cloud, which might had been caused by the combination of clouds and

190   precipitation. The AEF anomaly of larger amplitude appeared between 13:00 and 15:00 on 24 August, with almost no precipitation, CBH less than 1.5 km and LCC less than 0.1. However, the influences of TP and cloud cover were much pronounced at this time, but the AEF did not show any negative anomaly. Hence, a mixture of meteorological and seismic activity was considered as a possible cause of the negative anomaly on 24 August. Two negative AEF anomalies appeared on 26 August, from 00:00 to 12:00 and from 21:00 to 23:00. In the period of first AEF anomalies,

195   there was a prolonged small amount of TP, with a gradual rise in LCC, and a sudden increase in TP after the negative anomaly disappeared, which means that the AEF anomaly was probably resulted from the persistent precipitation washing away positive ions aground. The second segment of the AEF showed a decreasing trend at 21:00 and reached a minimal value at 22:30, returning to the FW-AEF level half an hour later, during which the LCC was close to zero and there was no TP, which was basically in line with the FW-AEF conditions. Hence, the second AEF anomalies on

200   26 August could be attributed to seismic activity.

For LES, the AEF anomaly appeared on 22 August between 20:00 and 23:00, with no precipitation and no low clouds existed, and the CBH was greater than 2 km throughout the whole day, which fully met the criteria for the

FW-AEF. Near-zero precipitation and no low clouds existed during the period of AEF anomaly occurring between 18:00 and 19:00 on 24 August. The negative anomalies appeared on 2 and 5 September both appeared between 08:00 and 12:00, with LCC less than 0.1 during the anomalies, but with high precipitation before and slightly higher precipitation after the anomalies. There was no TP and LCC on 5 September, with the CBH greater than 4 km all day. Therefore, it can be determined that the negative AEF anomalies appeared on 22 and 24 August, and 5 September might had been influenced by seismic activity, while the negative AEF anomaly appeared on 2 September could be attributed to the mixture of meteorological and seismic activity.
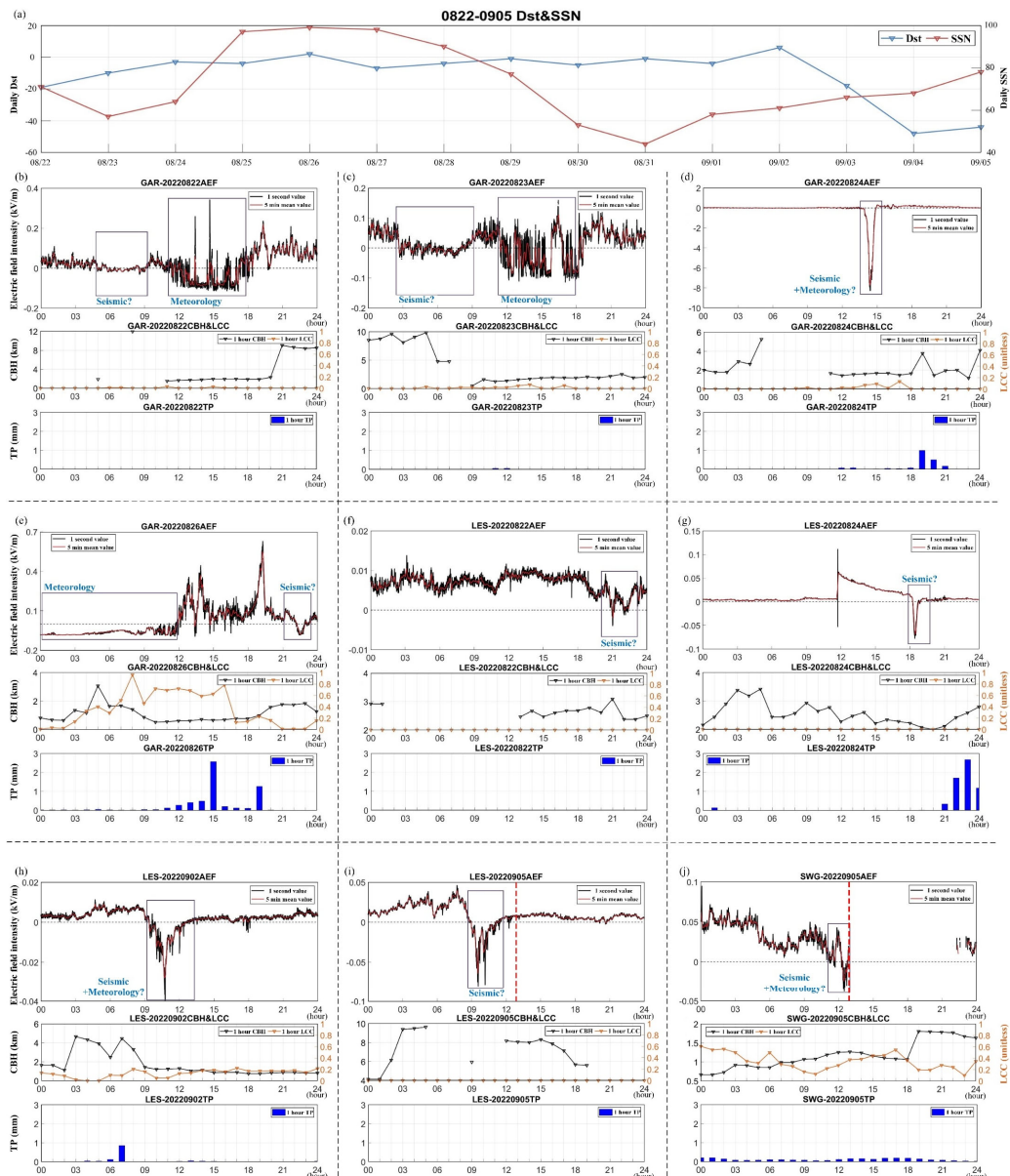
Figure.3 Changes in daily means of *Dst* and *SSN* from 22 August to 5 September (a). Nine negative AEF anomalies possibly related to

the Luding EQ and hourly meteorological parameters (including CBH, LCC, TP) for the corresponding time periods (b-j).

For SWG, the AEF on 5 September showed a downward trend from 04:00, dropping to a negative level at around 12:15, and the negative state lasted for 35 minutes until 12:50, reaching a minimal value of -0.04 kV m^{-1} at 12:29.

215 Due to the proximity of the site to the epicenter, the EQ triggered a power outage in the adjacent area, resulting in a data missing at SWG after 12:53. The site had light rain all day, with precipitation less than 0.2 mm, CBH greater than 500 m and LCC less than 0.6. However, as compared to the FW-AEF at the SWG, it can be found that the decreasing trend of AEF from 04:00 to 09:00 coincided perfectly with the simultaneous FW-AEF changes, and there was no significant change in magnitude, so the effect of meteorological activity on AEF on 5 September was not

220 particularly significant. In summary, the negative AEF anomaly appeared between 12:00 and 13:00 could be attributed to a combination of meteorological and seismic activity. Details of each parameter related with the AEF negative anomalies are shown in Table 3.

Table 3. Details of each parameter of the anomalous AEF time periods.

Site	Time period of AEF anomalies	CBH (km)	LCC (unitless)	TP (mm)
GAR	8/22 05:00-09:00	>10	0	0
GAR	8/23 03:00-08:00	>5	0	0
GAR	8/24 13:00-15:00	>1.5	<0.1	<0.01
GAR	8/26 21:00-23:00	>1.8	<0.01	0
LES	8/22 20:00-23:00	>2	0	0
LES	8/24 18:00-19:00	>2	0	<0.01
LES	9/02 09:00-12:00	>1	<0.1	<0.01
LES	9/05 08:00-11:00	>6	0	0
SWG	9/05 12:00-13:00	>1	<0.2	<0.1

4 Verification and Scrutinization

225 The variation in AEF, maintained by global thunderstorm activity, depends fundamentally on the concentration of near-surface atmospheric ions. Atmospheric ions are always present in the atmosphere on the fair-weather day and its presence gives the atmosphere with electrical conductivity. Rainfall, transit low clouds, haze and aerosols can all alter the concentrations of atmospheric ion directly or indirectly. It is necessary to understand clearly why the near-surface ion concentrations changed before the EQ, thus to reveal the intrinsic correlation of the pre-seismic AEF

230 anomalies to the Luding EQ.

4.1 P-holes manifestation verified by MBT, SSM and Geology

Some researchers explained well the reasons for positive MBT anomalies preceding EQs from the perspective of P-hole theory (Qi et al., 2021; Ding et al., 2022), and the AEF anomaly was mentioned in the conceptual diagrams of LCAI coupling process. Mao et al. (2020) demonstrated that the microwave dielectric constant decreases on rock

235 surfaces under compressive loading experimentally. Qi et al. (2021) discovered the positive MBT anomaly preceding the May 2008 Wenchuan EQ, and explained the geological preference of the positive MBT anomaly based on P-hole theory. When P-holes are transferred to the surface, it not only changes the dielectric constant, but also causes air ionization near the surface. According to the researches on seismic MBT anomalies in the same area of this study, MBT at the low frequency with horizontal polarization performed better (Qi et al., 2021, 2023). Therefore, MBT data

240 at 10.65 GHz with H polarization was selected, and the MBT anomalies during 15d before the Luding EQ were obtained by the spatio-temporally weighted two-step method (Qi et al., 2020) to analyze the potential surface microwave dielectric changes caused by the seismicity. Theoretically, MBT depends largely on the surface emissivity,

which lies on the dielectric constant and the physical temperature (Ulaby et al.,1981). The surface dielectric constant will increase and results in the decrease in MBT when SSM rises. Temperature changes, precipitation processes, and

245 the rise and fall of the underground water level all lead to changes in SSM, which can affect MBT. In order to identify seismic MBT anomalies, it is necessary to use SSM data to discriminate the MBT anomalies. In this research, SSM residuals from the surface to 10 cm underground were obtained by subtracting the average value of the same time period of the background year from the seismic year data, so as to discriminate the local drought factor.

Figure 4 shows residual MBT and residual SSM images from 22 August to 5 September, 2022. Overall, the positive

250 MBT anomalies in the study area were mainly concentrated in the plains to the east of the LMSF, the mountainous areas to west and northwest of the XSHF (mainly bare land), and the southeast corner of the Bayan Har Block, from 22 August to 1 September. Positive MBT anomalies gradually appeared in various areas on 22 August, with its range expanded to the maximum on 25 August and amplitude reaching to 10~15 K. The positive MBT anomalies still existed in few areas after 28 August, and generally dissipated after 2 September. The residual SSM remained a lower

255 value in most of the regions from 22 to 28 August, and there was also a significant increase on 30 August and a slow decline on the coseismic day. Therefore, the positive MBT anomalies due to local drought factors (SSM drop) should be excluded hereinafter. In details, the areas of positive MBT anomalies were distinguished by dashed polygons with different colors in Figure 4. The sequential positive MBT anomalies were zoned as zone I~VII, whose spatial relations to the surface lithology were shown in Figure 5.

260
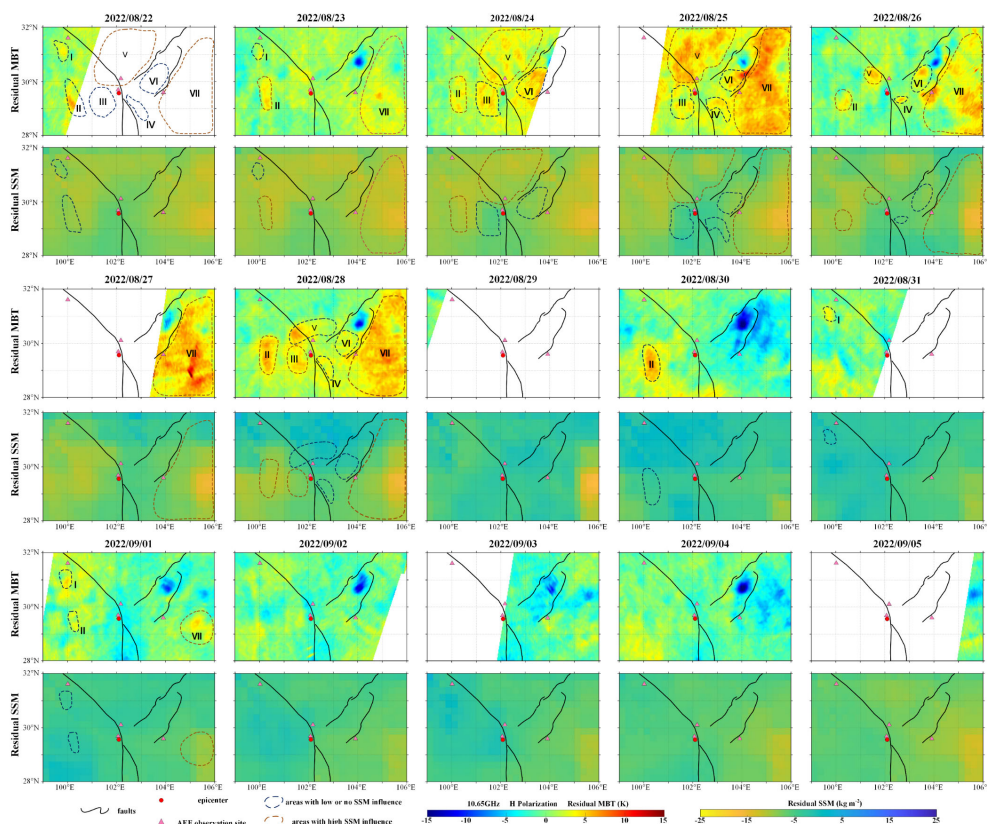
Figure 4. Residual MBT images at 10.65 GHz with H polarization and residual SSM from 22 August to 5 September. Blue polygons represent relatively low or no change in SSM while red polygons represent a significant drop in SSM.
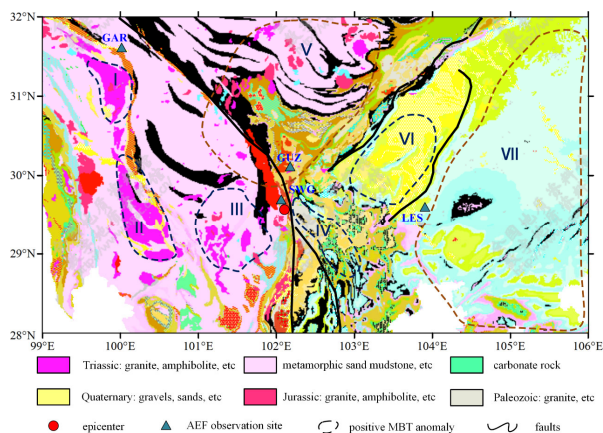
Figure 5. Distribution of surface lithology in the study area (data from the National Geological Archive).

265 Zone I was in the northwest corner of the study area, near Ganzi section of the XSHF. The MBT anomaly in zone I appeared on 22 August with an amplitude of 8 K (14d before the EQ), followed by a gradual decrease until 28 August. It appeared again on 31 August, with the positive anomaly spreading southward on 1 September and dissipating after 2 September (3d before the EQ). SSM residuals in zone I decreased by a lower amount than the surrounding area from 22 to 28 August, and remained almost unchanging after 31 August. The residual MBT and
270 SSM did not conform in time to the physical process that SSM decrease leads to the rise of MBT. Likewise, the spread of the positive MBT anomaly to the north on 28 August and the persistence of the MBT anomaly on 30 August in zone II cannot be explained by SSM change either.

The MBT anomalies in zone III were generally striped along XSHF, which started to appear on 23 August (13d before the EQ), with its amplitude increasing on 24 August, basically dissipating on 26 August. The MBT anomalies
275 appeared again on 28 August with the maximum amplitude of about 10 K, then gradually weakened before the EQ. The residual SSM in zone III was low on 23 and 24 August, which was inconsistent with the amplitude increase in MBT anomaly. A small decrease in SSM residuals appeared in zone III on 28 August, which was consistent with the appearance of the positive MBT anomaly. There was a good spatio-temporal correlation between the positive MBT anomaly and SSM decline.

280 Positive MBT anomalies in zone IV gradually became apparent on 24 August, more pronounced in the north on 26 August and in the south on 28 August. The SSM residuals were in a state of low negative value from 24 to 28 August and no significant change was detected over time. This was also the case for zone VI, where the variation in SSM was slight during the MBT anomalies from 24 to 28 August. The positive MBT anomalies in zone V mainly appeared on 24 and 25 August, with a large range of high amplitude. The SSM in zone V decreased during the same period,
285 and then SSM residuals gradually increased, which corresponded well with the positive MBT anomalies on the space and time scales. The same situation also happened in zone VII as for zone V from 23 to 31 August.

After analyzing the spatio-temporal evolution of MBT and SSM residuals in the seven zones of MBT anomalies, the appearance of positive MBT anomalies in five zones (I, II, III, IV and VI) were thought to be related to the Luding EQ. Accordingly, the positive MBT anomalies associated with seismic activity in these five zones were further
290 analyzed by introducing the lithology distribution map and numerical simulations of the CSFA. Figure 5 shows the surface lithology in the study area. According to P-hole theory, the production and convergence of P-holes occurs in rocks with peroxy-deficient (peroxy-bonded) structures, and the main carriers of peroxy-bonded are low-crystalline minerals including quartz and feldspar (Freund, 2002). As can be seen in Figure 5, the lithology of zone I, II and III

is dominated by granites, metamorphic sandstones and other rocks containing quartz and feldspar components with
295   peroxide defect structures. Zone VI is dominated by the Quaternary, the geological strata is relatively loose and the
major lithology is sand and gravel consisting of granular quartz, feldspar, mica, etc. Zone IV has a more complex
lithological distribution behaving fewer minerals with peroxy-deficient structure than the others, and the appearance
of positive MBT anomalies in zone IV were shorter in duration and relatively small in area. Therefore, it was
considered that zones I, II, III and VI are more prone to positive MBT anomalies following P-hole aggregation.

300   The uneven distribution of crustal stress and its gradually accumulation are the main causes of tectonic seismicity.
Based on the Crust 2.0 model and stratigraphic data (Shan et al., 2009; Li et al., 2022), a three-dimensional (3D)
stratigraphic model was constructed using the 3D finite element method to simulate the CSFA due to seismic tectonics
at a time scale of 1000 years. The stratigraphic model had an east-west width of 1000 km, a north-south width of 800
km and a depth of 83 km, and the simulated crustal stress within the study area of this research was intercepted
305   (Figure 6). Historical EQ catalogs from 1770 to 2022 were selected to make seismic validation of the simulated CSFA.
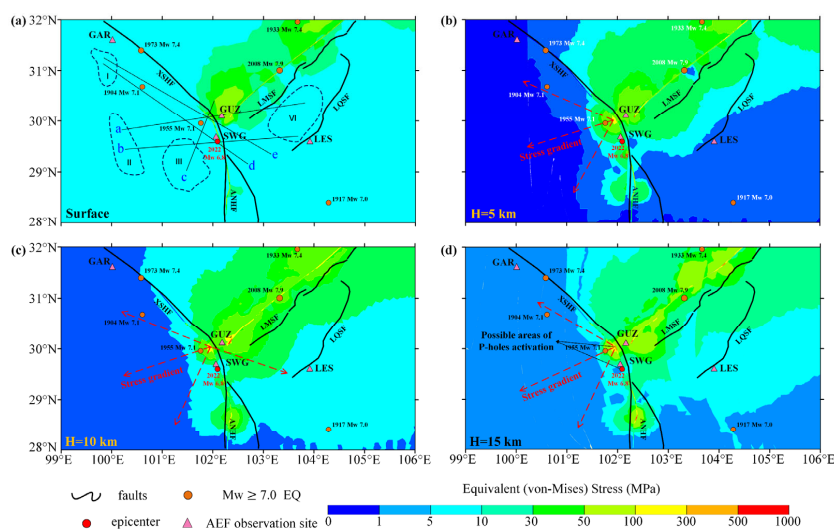
Figure 6. Spatial distribution of equivalent stress at ground surface (a), 5 km deep (b), 10 km deep (c) and 15 km deep (d).

As shown in Figure 6, the equivalent stress intercepted at different depths was used to reflect the crustal stress
background. In the map of the CSFA at the depth of 15 km, crustal stress was mainly concentrated in three places,
310   i.e., the left side of the southeast section of XSHF, the area along LMSF and the right side of ANHF. Large EQs
(magnitude of 7 or higher) had occurred in all the three places in history. The activated P-holes are to flow from the
seismic source area to upper crust in response to the stress gradients (St-Laurent et al., 2006). Compared with the
stress concentration areas at the depth of 15 km, the size of the surface stress concentration areas as well as the stress
magnitude are weakened, indicating that there was an overall upward stress gradient between the 15 km depth plane
315   and the ground surface.

In addition, the high stress areas are mainly concentrated in the central study area as well as in the northeast, with
lower stress appearing in the southeast and southwest, indicating the existence of a stress gradient toward the
southeast and west sides. P-holes generation would occur not only at the hypocenter, but also in areas of high stress
concentration. Based on the simulated CSFA, the hypocenter and its nearby high stress area were selected as the
320   places where the P-holes activations were generated, at a depth of 15 km about. The stress gradients from the
hypocenter or the nearby high stress area to the four seismic MBT zones were calculated by dividing the stress

difference by the distance. The results are shown in Table 4, and the corresponding stress profiles are described in Figure 7. P-holes could be activated from the hypocenter or from its nearby high stress area, thus there was the possibility of P-holes transferring along the stress gradient to all the four seismic MBT regions. It is also clear that

325   the closer to the hypocenter or the high stress area, the higher the stress gradient.
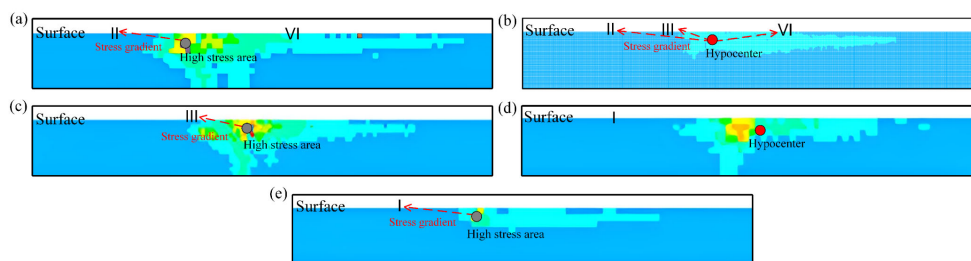
Figure 7. The vertical sections of crustal stress from the hypocenter or nearby high stress area to the four seismic MBT zones. Subplot (b) and (d) are vertical profiles through the hypocenter, while subplot (a), (c) and (e) are the vertical profile started from the nearby high stress concentration areas.

330   **Table 4.** Stress gradients from two P-hole activation areas to the four residual MBT regions in Figure 4.

Zones	Stress magnitude (MPa)	Distance to epicenter (km)	Distance to high stress area (km)	Stress gradient from hypocenter	Stress gradient from high stress area
I	18.72	259.09	219.53	0.41	76.45
II	14.73	190.46	183.22	0.58	91.62
III	18.50	88.57	109.88	1.20	152.73
VI	58.74	162.18	181.92	0.41	92.02

In summary, the positive MBT anomalies that appeared in zones I, II, III, and VI during 14d before the EQ were identified to be related to seismic activity. Positive MBT anomalies in ground surface due to CSFA indicates the occurrence of P-hole aggregation, which provides the conditions for air ionization to exist in the near-surface atmosphere.

335   **4.2 Scrutinization of seismic AEF anomalies**

For the screened negative AEF anomalies, there was a certain difference in space and time between the sites and the positive MBT anomaly regions. Therefore, it should be considered that positive ions generated by P-hole ionized air can spread in the atmosphere and drift to the sites with the wind field. Based on the near-surface wind direction and wind speed, whether there was a suitable wind field between the site and the positive MBT anomaly regions can

340   be determined. In this study, the data of wind field at 10 m aground with a temporal resolution of 1 hour were used. Since the wind speed in the whole study area was less than 8 m s^{-1}, the distance of atmospheric ions transported by the wind field was very limited, as a result of neutralization due to electrostatic action and absorption of aerosol (Wright, et al., 2020). Therefore, only the wind field in the zone of positive MBT anomaly nearest to the AEF sites were considered.

345   The occurrence of negative AEF anomalies can be divided into two categories. The first one is that the wind field in the MBT anomaly area did not show a trend moving towards the AEF site, such as the negative AEF anomaly at GAR on 22, 23 and 26 August, and LES on 24 August and 2 September. In Figure 8(a), the times of MBT residual and SSM residual images were both 02:00 on 22 August, and the wind direction and speed were at four moments of 03:00, 05:00, 07:00 and 09:00. The wind direction from zone I to GAR was not indicated before and during the MBT

anomaly, and the wind speed was too low to transfer the positive ions generated on the ground surface in zone I to GAR, thus the negative AEF anomaly at GAR on that day was not resulted from seismic activity. The other four days were all in the same situations as this day.
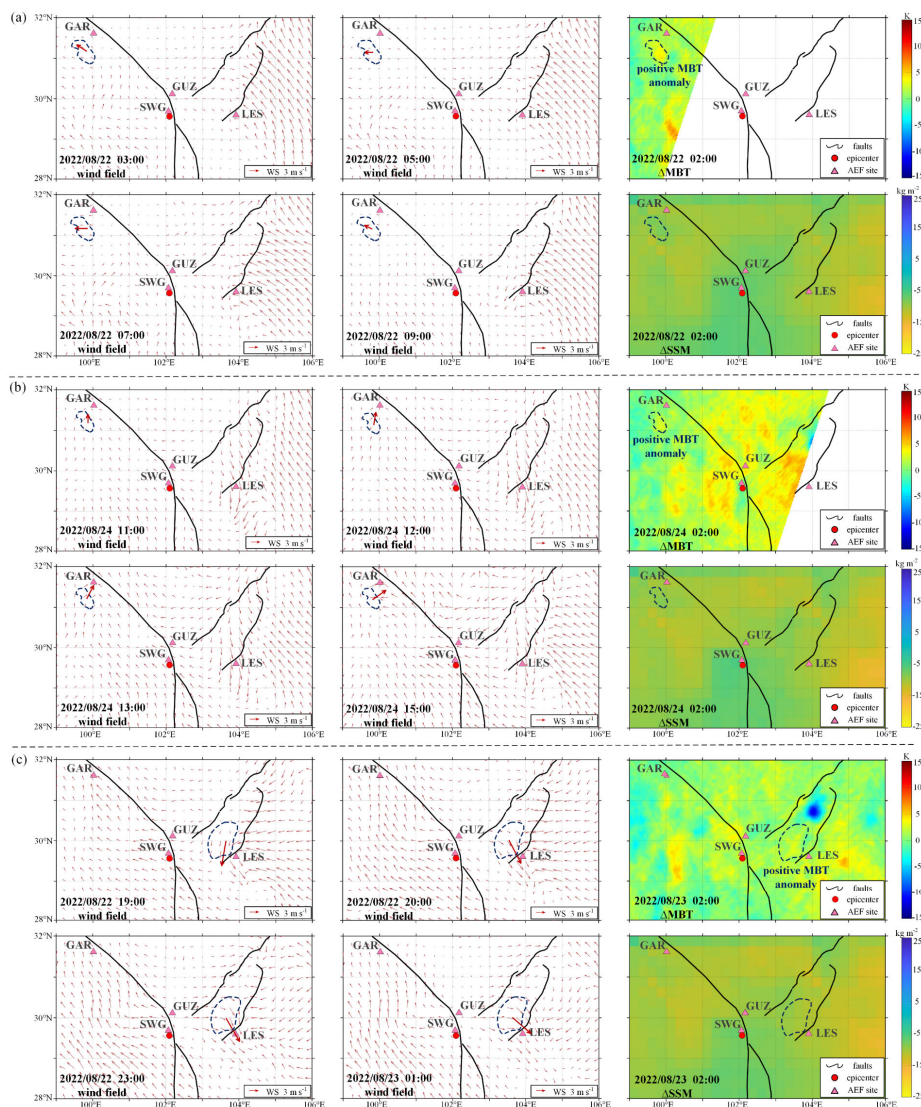
Figure 8. Wind field, MBT residuals and SSM residuals in the study area on 22 August (a) and 24 August (b) for GAR, and on 22 August for LES (c), 2022.

The second category is that the wind field in the area of positive MBT anomalies was pointed towards the AEF sites, such as the negative AEF anomalies at GAR on 24 August and LES on 22 August. In Figure 8(b), the AEF anomaly at GAR appeared between 13:00 and 15:00 on 24 August. Before 11:00, the wind direction in zone I was slightly to the west of the site, the wind direction began to deflect to the northeast at 12:00 with the direction pointing to the site and keeping the direction until 14:00, during which the wind speed gradually increased. The wind deflected

to the northeast again at 15:00, and then gradually deviated. The wind field changes during this period coincided well with the appearance of the negative AEF anomaly, and the wind field at the site in the end of the anomaly period was also changing, so a longer period of AEF anomaly caused by positive ions staying and accumulating at the site could be ruled out, which was also consistent with the AEF returning to positive levels after 15:00. Therefore, it can be

365 assumed that the negative AEF anomaly at GAR on 24 August had been influenced by seismic activity. In Figure 8(c), the AEF anomaly appeared between 20:00 and 23:00 on 22 August at LES. The wind field was pointing west of the AEF site before the anomaly appeared, and then veered east and pointed towards the site from 20:00 to 23:00. Then, the wind field continued to veer east and drifted away from the site at 01:00 the next morning. The changes in wind field corresponded well to the time of the appearance of the negative AEF anomaly, which shows that seismic

370 activity might had impacted on the AEF anomaly at that time.

On the coseismic day, although there were AEF anomalies appeared at the LES and SWG, the MBT data were missing due to satellite coverage. Considering that the surface lithology at the two sites was similar to that of the nearest MBT anomaly area, plus the negative AEF anomaly appeared only 4 hours before the EQ, it can be inferred that a localized P-hole aggregation phenomenon might had appeared in the very local area as a direct result of seismic

375 activity, causing air ionization so as to alter the vertical AEF.

In conclusion, the negative AEF anomalies at GAR from 13:00 to 15:00 on 24 August and at LES from 18:00 to 19:00 on 22 August were considered to be associated with the surface P-hole accumulation resulted from seismic activity. The anomalous AEF signals at LES and SWG 4 hours before the EQ on 5 September were considered to be related to the localized changes in atmospheric ion concentrations due to seismic activity in the short imminent stage

380 of the Luding EQ.

5 Conclusions

In this research, the historical AEF data from four AEF sites at GAR, LES, GUZ, and SWG were obtained to construct and analyze the FW-AEF, which were in positive fluctuation states and characterized by single or double peaks. Then, the AEF variations during 15d before the Luding EQ in 2022 were carefully checked, using FW-AEF

385 as a reference. Accordingly, nine AEF negative anomalies (four at GAR, four at LES and one at SWG) were considered to be potentially related to the Luding EQ, by analyzing the meteorological parameters including CBH, LCC, TP, and space weather parameters including *Dst* and *SSN*. Furthermore, the MBT residuals during 15d before the Luding EQ were jointly analyzed with SSM, geological maps, and numerically simulated CSFA, to confirm the existence of conditions that alter the atmospheric ion concentration in the study area. The geophysical environment

390 for high-stress concentration in crust, positive charge carriers transfer and accumulation to ground were proved by the numerical simulation, which all satisfied the production of seismic AEF anomalies. Furthermore, the ground-based wind field data were used to explore the reasons of the negative AEF anomalies under the premise of spatial differentiation between AEF sites and positive charge carrier accumulation areas. The confirmed causes of the AEF anomalies reported in the study are listed in Table 5.

395 **Table 5.** Summary of the AEF anomalies before the Luding EQ on 5 September, 2022.

AEF sites	Duration of AEF anomalies	Presence of meteorological effect	Presence of seismic effect	Causes of negative AEF anomalies
GAR	8/24 13:00-15:00	√	√	seismic and meteorological effects
GAR	8/26 21:00-23:00	√	×	meteorological effect
LES	8/22 20:00-23:00	×	√	seismic effect
LES	9/02 09:00-12:00	√	×	meteorological effect
LES	9/05 08:00-11:00	×	√	seismic effect

SWG	9/05 12:00-13:00	√	√	seismic and meteorological effects

The negative seismic AEF anomalies preceding the Luding EQ were attributed to the positive charge carriers produced in high stress concentration areas and accumulated on ground surface, which were able to ionize the near surface air of the surrounding atmosphere. This provides a bridge to establishing the coupling process between coversphere and atmosphere for understanding multiple seismic anomalies. The jobs of identifying and judging seismic AEF anomalies reported in this study is expected to provide a typical example for future research.

Data availability

All data can be provided by the corresponding authors upon request.

Author contributions

LW, XW and YQ designed the framework of the manuscript; XW and YQ wrote the manuscript draft; LW and YQ polished the manuscript; JL and WM performed the mechanical simulation; XW and JL completed the visualization, LW provided the funding. All authors have read and agreed to the published version of the manuscript.

Competing interests

The authors declare that they have no conflict of interest.

Financial support

This work was supported by the Key Program of National Nature Science Foundation of China (41930108).

References

Chen, C. H., Sun, Y. Y., Lin, K., Zhou, C., Xu, R., Qing, H., Gao, Y., Chen, T., Wang, F., Yu, H., Han, P., Tang, C. C., Su, X., Zhang, X., Yuan, L., Xu, Y., and Liu, J.Y.: A new instrumental array in Sichuan, China, to monitor vibrations and perturbations of the lithosphere, atmosphere and ionosphere, Surv. Geophys., 42, 1425–1442, https://doi.org/10.1007/s10712-021-09665-1, 2021.

Chen, T., Wang, S. H., Li, L., Yang, M. P., Zhang, L. Q., Zhang, X. M., Huang, P. Q. Liu, J., Xiong, P., Ti, S., Wu, H., Song, J. J., Wang, C., Su, J. F., and Luo, J.: Analysis of abnormal signal of atmospheric electric field before the 2021-04-16 Luanzhou MS4.3 Earthquake in Hebei Province, J. Geodesy and geodynamics., 42, 771-776, https://doi.org/10.14075/j.jgg.2022.08.001, 2022.

Ding, Y. F., Qi, Y., Wu, L. X., Mao, W. F., and Liu, Y. J.: Discriminating the multi-frequency microwave brightness temperature anomalies relating to 2017 Mw 7.3 Sarpol Zahab (Iran-Iraq border) earthquake, Frontiers Earth. Sci., 9, 656216, https://doi.org/10.3389/feart.2021.656216, 2021.

Freund, F.: Time-resolved study of charge generation and propagation in igneous rocks, J. Geophys. Res.: Solid Earth, 105, 11001-11019, https://doi.org/10.1029/1999JB900423, 2000.

Freund, F.: Charge generation and propagation in igneous rocks, J. Geodyn., 33, 543-570, https://doi.org/10.1109/10.1029/1999JB900423, 2002.

Freund, F.: Toward a unified solid state theory for pre-earthquake signals, Acta Geophysica, 58, 719-766, https://doi.org/10.2478/s11600-009-0066-x, 2010.

Freund, F.: Earthquake forewarning — A multidisciplinary challenge from the ground up to space, Acta Geophysica, 61, 775-807, https://doi.org/10.2478/s11600-013-0130-4, 2013.

Hao, J. G.: Near-surface atmospheric electric field anomalies and earthquakes, Acta Seismologica Sinica, 02, 206-212+226, 1988.

Harrison, R. G., and Nicoll, K. A.: Fair weather criteria for atmospheric electricity measurements, J. Atmos. Sol.-Terr.

Phys., 179, 239-250, https://doi.org/10.1016/j.jastp.2018.07.008, 2018.

440   Hersbach, H., Bell, B., Berrisford, P., Biavati, G., Horányi, A., Muñoz Sabater, J., Nicolas, J., Peubey, C., Radu, R., Rozum, I., Schepers, D., Simmons, A., Soci, C., Dee, D., Thépaut, J-N.: ERA5 hourly data on single levels from 1940 to present. Copernicus Climate Change Service (C3S) Climate Data Store (CDS), https://doi.org/10.1109/10.24381/cds.adbb2d47, 2023.

        Yasuhide, H., Mako, W., Risa, M., Hiroshi, K., Takuo, T., and Masashi, H.: On the Spatio-temporal dependence of

445   anomalies in the atmospheric electric field just around the time of earthquakes, Atmosphere., 13, 1619, https://doi.org/10.3390/atmos13101619, 2022.

        Imaoka, K., Maeda, T., Kachi, M., Kasahara, M., Ito, N., and Nakagawa, K.: "Status of AMSR-2 Instrument on GCOM-W1," in Earth Observing Missions and Sensors: Development, Implementation, and Characterization II, International Society for Optics and Photonics, Japan, 8528, 852815, 2012.

450   Israelsson, S., and Tammet, H.: Variation of fair weather atmospheric electricity at Marsta Observatory, Sweden, 1993–1998, J. Atmos. Sol.-Terr. Phys., 63, 1693-1703, https://doi.org/10.1016/S1364-6826(01)00049-9, 2001.

        Ji, L. Y., Zhang, W. T., Liu, C. J., Zhu, L. Y., Xu, J., and Xu, X. X.: Characterizing interseismic deformation of the Xianshuihe fault, eastern Tibetan Plateau, using Sentinel-1 SAR images, Adv Space Res, 66, 378-394, https://doi.org/10.1016/j.asr.2020.03.043, 2020.

455   Ji, Z. R.: FPGA-based design of an atmospheric electric field meter, M. S. thesis, Nanjing University of Information Science and Technology, China, 73 pp., https://doi.org/10.27248/d.cnki.gnjqc.2022.000465, 2022.

        Jin, X. B., Zhang, L., Bu, J. W., Qiu, G. L., Ma, L., Liu, C., and L, Y. D.: Discussion on anomaly of atmospheric electrostatic field in Wenchuan Ms8.0 earthquake, J. Electrost., 104, 103423, https://doi.org/10.1016/j.elstat.2020.103423, 2020.

        Kleimenova, N. G., Kozyreva, O. V., Michnowski, S., and Kubicki, M.: Effect of magnetic storms in variations in the

460   atmospheric electric field at midlatitudes, Geomagn. Aeron., 48, 622-630, https://doi.org/10.1134/S0016793208050071, 2008.

        Kondo, G.: The variation of the atmospheric electric field at the time of earthquake, Mem. Kakioka Magnet. Observ., 12, 11-23, 1966.

        Li, L.: Atmospheric electric field data before 2022 Ms 6.8 Luding earthquake [DS/OL]. V1. Science Data Bank,

465   https://doi.org/10.57760/sciencedb.o00009.00237, 2022.

        Li, Y. C., Zhao, D. Z., Shan, X. J., Gao, Z. Y., Huang, X., and Gong, W. Y.: Coseismic Slip Model of the 2022 Mw 6.7 Luding (Tibet) Earthquake: Pre-and Post-Earthquake Interactions With Surrounding Major Faults, Geophys Res Lett, 49, e2022GL102043, https://doi.org/10.1029/2022GL102043, 2022.

        Li, Y. D., Zhang, L., Zhang, K., and Jin, X. B.: A study on the anomalies of near-surface atmospheric electric field before

470   the "5.12" Wenchuan Earthquake, Plateau and Mountain Meteorology Res., 37, 49-53, https://doi.org/10.3969/j.issn.1674-2184·2017.01.008, 2017.

        Mao, W. F., Wu, L. X., Liu, S. J., Gao, X., Huang, J. W., Xu, Z. Y., and Qi, Y.: Additional microwave radiation from experimentally loaded granite covered with sand layers: Features and mechanisms, IEEE Trans. Geosci. Remote Sens., 58, 5008–5022, https://doi.org/10.1109/TGRS.2020.2971465, 2020.

475   Omori, Y., Yasuoka, Y., Nagahama, H., Kawada, Y., Ishikawa, T., Tokonami, S., and Shinogi, M.: Anomalous radon emanation linked to preseismic electromagnetic phenomena, Nat. Hazard. Earth Syst. Sci., 7, 629-635, https://doi.org/10.5194/nhess-7-629-2007, 2007.

        Qi, Y., Wu, L., He, M., and Mao, W.: Spatio–temporally weighted two step method for retrieving seismic MBT anomaly: May 2008 Wenchuan earthquake sequence being a case, IEEE J. Sel. Topics Appl. Earth Observ. Remote Sens., 13,

480   382–391, https://doi.org/10.1109/JSTARS.2019.2962719, 2020.

        Qi, Y., Wu, L.X., Mao, W. F., Ding, Y. F., and He, M.: Discriminating possible causes of microwave brightness temperature positive anomalies related with May 2008 Wenchuan earthquake sequence, IEEE Trans. Geosci. Remote Sens., 59,

1903-1916, https://doi.org/10.1109/TGRS.2020.3004404, 2021a.

Qi, Y., Wu, L., Ding, Y., Liu, Y., Chen, S., Wang, X., and Mao, W. F.: Extraction and discrimination of MBT anomalies possibly associated with the Mw 7.3 Maduo (Qinghai, China) Earthquake on 21 May 2021, Remote Sens., 13, 4726, https://doi.org/10.3390/rs13224726, 2021b.

Qi, Y., Wu, L. X., Ding, Y. F., and Mao, W. F.: Microwave brightness temperature anomalies associated with the 2015 Mw 7.8 Gorkha and Mw 7.3 Dolakha earthquakes in Nepal, IEEE Trans. Geosci. Remote Sens., 60, 1-11, https://doi.org/10.1109/TGRS.2020.3036079, 2022.

Qi, Y., Wu, L. X., Mao, W. F., Ding, Y., Liu, Y., Wang, X.: Characteristic background of microwave brightness temperature (MBT) and optimal microwave channels for searching seismic MBT anomaly in and around the Qinghai-Tibet Plateau, IEEE Trans. Geosci. Remote Sens., https://doi.org/ 10.1109/TGRS.2023.3299643, 2023.

Qin K., Wu L. X., Zheng S., and Liu S. J.: A Deviation-Time-Space-Thermal (DTS-T) Method for Global Earth Observation System of Systems (GEOSS)-Based Earthquake Anomaly Recognition: Criterions and Quantify Indices. Remote Sens., 5, 5143-5151, https://doi.org/10.3390/rs5105143, 2013.

Rodell, M., Houser, P. R., Jambor, U. E. A., Gottschalck, J., Mitchell, K., Meng, C. J., Arsenault, K., Cosgrove, B., Radakovich, J., Bosilovich, M., Entin, J. K., Walker, J. P., Lohmann, D., and Toll, D.: The global land data assimilation system, Bull. Am. Meteorol. Soc., 85, 381-394, https://doi.org/10.1175/BAMS-85-3-381, 2004.

Rycroft, M. J., Israelsson, S., and Price, C.: The global atmospheric electric circuit, solar activity and climate change, J. Atmos. Sol.-Terr. Phys., 62, 1563-1576, https://doi.org/10.1016/S1364-6826(00)00112-7, 2000.

Shan, B., Xiong, X., Zheng, Y., and Diao, F. Q.: Stress changes on major faults caused by M w7. 9 Wenchuan earthquake, May 12, 2008, Science in China Series D: Earth Sci., 52, 593-601, https://doi.org/10.1007/s11430-009-0060-9, 2009.

Smirnov, S.: Negative anomalies of the earth's electric field as earthquake precursors, Geosciences, 10, 10, https://doi.org/10.3390/geosciences10010010, 2019.

St-Laurent, F., Derr, J. S., and Freund, F. T.: Earthquake lights and the stress-activation of positive hole charge carriers in rocks, Phys Chem Earth. Parts A/B/C, 31, 305-321, https://doi.org/10.1016/j.pce.2006.02.003, 2006.

Sun, J. Q.: Fundamentals of atmospheric electricity, China Meteorological Press., 1987.

Tacza, J., Raulin, J. P., Mendonca, R. S., Makhmutov, V. S., Marun, A., and Fernandez, G.: Solar effects on the atmospheric electric field during 2010–2015 at low latitudes, J. Geophys. Res. Atmos., 123, 11970-11979, https://doi.org/10.1029/2018JD029121, 2018.

Ulaby, F. T., Moore, R. K., and Fung, A. K.: Microwave Remote Sensing: Active and Passive. in Remote Sensing Fundamentals and Radiometry, Addison-Wesley, USA, 186–254.

Wu, L. X., Qi, Y., Mao, M. F., Lu, J. C., Ding, Y. F., Peng, B. Q., and Xie, B. S.: Scrutinizing and rooting the multiple anomalies of Nepal earthquake sequence in 2015 with the deviation–time–space criterion and homologous lithosphere–coversphere–atmosphere–ionosphere coupling physics, Nat. Hazard. Earth Syst. Sci., 23, 231-249, https://doi.org/10.5194/nhess-23-231-2023, 2023.

Wu L. X. and Liu S. J.: Remote Sensing Rock Mechanics and Earthquake Infrared Anomalies. In: Advances in Geosciences & Remote Sensing; Gary J, Ed., InTech: Vukovar, Croatia, 709–741, 2009.

Wu L. X., Qin K, and Liu S. J.: GEOSS-based Thermal Parameters Analysis for Earthquake Anomaly Recognition. Proc. of IEEE, 100, 2891-2907, https://doi.org/10.1109/JPROC.2012.2184789, 2012.

Wright, M. D., Matthews, J. C., Silva, H. G., Bacak, A., Percival, C., and Shallcross, D. E.: The relationship between aerosol concentration and atmospheric potential gradient in urban environments, Sci Total Environ, 716, 134959, https://doi.org/10.1016/j.scitotenv.2019.134959, 2020.

Yang, W., Liu, J., Xie M. Y., Zang, Y., Meng, L. Y., and Zhang, X. M.: Study on relocation of the September 5, 2022 Luding Ms6. 8 earthquake, Earth. Res. China, 38, 622-631, https://doi.org/10.3969/j.issn.1001-4683, 2022.